Injectable Colloidal Gold for Use in Intrafractional 2D Image-Guided Radiation Therapy

Jølck, Rasmus Irming; Rydhog, Jonas S.; Christensen, Anders Nymark; Hansen, Anders Elias; Bruun, Linda Maria; Schaarup-Jensen, Henrik; von Wenck, Asger Stevner; Borresen, Betina; Kristensen, Annemarie T.; Clausen, Mads Hartvig; Kjær, Andreas ; Conradsen, Knut; Larsen, Rasmus; af Rosenschold, Per Munck; Andresen, Thomas Lars

Published in:
Advanced Healthcare Materials

Link to article, DOI:
10.1002/adhm.201400651

Publication date:
2015

Document Version
Publisher's PDF, also known as Version of record

FULL PAPER

Injectable Colloidal Gold for Use in Intrafractional 2D Image-Guided Radiation Therapy

*Rasmus I. Jølck, Jonas S. Rydhög, Anders N. Christensen, Anders E. Hansen, Linda M. Bruun, Henrik Schaarup-Jensen, Asger Stevner von Wenck, Betina Børresen, Annemarie T. Kristensen, Mads H. Clausen, Andreas Kjær, Knut Conradsen, Rasmus Larsen, Per Munck af Rosenschöld, and Thomas L. Andresen**

In the western world, approximately 50% of all cancer patients receive radiotherapy alone or in combination with surgery or chemotherapy. Image-guided radiotherapy (IGRT) has in recent years been introduced to enhance precision of the delivery of radiation dose to tumor tissue. Fiducial markers are often inserted inside the tumor to improve IGRT precision and to enable monitoring of the tumor position during radiation therapy. In the present article, a liquid fiducial tissue marker is presented, which can be injected into tumor tissue using thin and flexible needles. The liquid fiducial has high radiopacity, which allows for marker-based image guidance in 2D and 3D X-ray imaging during radiation therapy. This is achieved by surface-engineering gold nanoparticles to be highly compatible with a carbohydrate-based gelation matrix. The new fiducial marker is investigated in mice where they are highly biocompatible and stable after implantation. To investigate the clinical potential, a study is conducted in a canine cancer patient with spontaneous developed solid tumor in which the marker is successfully injected and used to align and image-guide radiation treatment of the canine patient. It is concluded that the new fiducial marker has highly interesting properties that warrant investigations in cancer patients.

1. Introduction

Nanomaterials offer unique properties that can provide society with new healthcare technologies for treatment of disease. With the increasing aging of the population in the western world, cancer incidence continues to rise creating a crucial demand for efficient and cost-effective therapies. Radiation therapy is a cost-effective treatment modality and approximately 50% of cancer patients receive radiation therapy after being diagnosed with cancer.[1] Modern radiation oncology relies on advanced, high-precision imaging techniques such as computed tomography (CT), positron emission tomography (PET), and magnetic resonance (MR) to enable the delivery of high radiation doses to defined targets.[2–4] However, tumors rarely display a fixed position during irradiation or within the treatment period

Dr. R. I. Jølck, Dr. A. E. Hansen, L. M. Bruun, Prof. T. L. Andresen
DTU Nanotech, Department of Micro-and Nanotechnology
Center for Nanomedicine and Theranostics
Technical University of Denmark
Building 345E, Ørsteds Plads,
2800 Lyngby, Denmark
E-mail: thomas.andresen@nanotech.dtu.dk

J. S. Rydhög, Dr. P. Munck af Rosenschöld
Department of Oncology
Section of Radiotherapy
3994, Rigshospitalet
Blegdamsvej 9, 2100 Copenhagen, Denmark

J. S. Rydhög, Dr. P. Munck af Rosenschöld
the Niels Bohr Institute, University of Copenhagen
Blegdamsvej 17, 2100 Copenhagen, Denmark

A. N. Christensen, Prof. K. Conradsen, Prof. R. Larsen
DTU Compute, Department of Applied Mathematics
and Computer Science
Technical University of Denmark
Building 321/324, Matematiktorvet, 2800 Lyngby, Denmark

H. Schaarup-Jensen, Prof. M. H. Clausen
DTU Chemistry
Department of Chemistry
Center for Nanomedicine and Theranostics
Technical University of Denmark
Building 207, Kemitorvet, 2800 Lyngby, Denmark

A. Stevner von Wenck, B. Børresen,
Prof. A. T. Kristensen
Department of Veterinary Clinical and Animal Sciences
Faculty of Health and Medical Sciences
University of Copenhagen
Dyrlægevej 16, 1870 Frederiksberg C, Denmark

Prof. A. Kjær
Department of Clinical Physiology
Nuclear Medicine & PET and Cluster for Molecular Imaging
Rigshospitalet and University of Copenhagen
Blegdamsvej 9, 2100 Copenhagen, Denmark

DOI: 10.1002/adhm.201400651

due to breathing motion, changes in organ filling, and tumor size.[5–7] To compensate for variations in tumor position frequent imaging (kilovoltage radiographs or fluoroscopy—also referred to as 2D X-ray imaging) during the course of treatment or image-guided radiation therapy (IGRT) is now being used in the clinic to improve radiation precision and accuracy, thereby reducing the treatment toxicity and optimizing therapeutic efficacy.[2,6,8] When the tumor position cannot be correlated with internal reference points such as the skeleton, tumor localization can be enhanced by alignment to radiographic markers implanted in or near the tumor.[9–11] Such markers can improve treatment through optimized planning, tumor positioning accuracy, and tumor tracking resulting in more precise dose delivery and enable treatment of cancers, which are presently not eligible for radiotherapy.[12,13] Tissue markers currently used in the clinic are metal-based solid implants with large physical dimensions, which require complicated insertion procedures and therefore the risk of complications. Lung tumor insertion is especially problematic, with pneumothorax (reported in 33%–68% of patients) as well as bleeding being reported as primary complications.[14–16] In order to increase the usability and patient compliance of radiographic markers, we recently described the concept of a liquid injectable fiducial marker by exploiting polyethylene glycol (PEG)-coated gold nanoparticles (AuNPs) in a nonsolvent-induced phase separation (NIPS) gelation matrix.[17] This system was found to be biocompatible and clearly visible on 3D X-ray imaging, However, due to the chemical properties of the encapsulated AuNPs only 10 mg AuNPs mL^{-1} providing approximately 200 Hounsfield units (HU) of contrast could be included, which is insufficient for 2D X-ray visualization. For gating-based radiation procedures, often exploited in for example lung cancer patients, 2D X-ray visualization is required for intrafractional real-time imaging of moving tumors.[6,18–20] Additionally, fiducial marker visualization using 2D X-ray techniques lowers the X-ray exposure level to the patients and may reduce treatment time compared to 3D X-ray-based procedures.[2] Furthermore, with the increasing focus on stereotactic radiation procedures and the clinical introduction of proton therapy, visualization of tumor position and motion becomes crucial to optimize irradiation of cancerous tissue.[21,22] Therefore, radiopaque fiducial markers continue to be in high demand and development of new marker systems is of paramount importance.

In the present work, we have investigated a novel liquid fiducial marker (nanogel) system based on sucrose acetate isobutyrate (SAIB) and uniform poly(*N*-isopropyl acrylamide) (PNIPAM)-coated AuNPs with radio-opacity adequate for 2D X-ray visualization. SAIB, a fully acylated derivative of sucrose, is a biodegradable nonpolymeric compound, which has been approved for oral consumption and is generally regarded as safe (GRAS) by the FDA. SAIB mixtures with ethanol (EtOH) behaves as Newtonian liquids and have a low viscosity (50–200 mPa s) suited for injection using thin hypodermic needles.[23–25] Upon hydration, an amorphous (gel-like) solid is formed, which efficiently encapsulate high concentrations (>100 mg Au mL^{-1}) of PNIPAM-coated AuNPs providing contrast levels sufficient for visualization in 2D X-ray imaging techniques such as fluoroscopy and ExacTrac imaging (Brainlab AG, Feldkirchen, Germany). The developed nanogel has been characterized in vitro and the in vivo stability and visibility was evaluated in immunocompetent mice over a period of 8 weeks. Proof-of-concept in a clinical canine cancer patient with a spontaneous growing tumor was additionally established and the developed nanogel with PNIPAM-coated AuNPs was applied in IGRT in a canine cancer patient where marker visibility, stability, and marker migration were evaluated over time during the course of radiotherapy. The developed nanogel fulfills the requirements for use in guidance of radiation therapy as it is easy to inject, remains stable over the full time course of radiation treatment (6 weeks), shows no sign of migration, and is the first liquid fiducial marker to enable visualization using both 2D and 3D X-ray-based imaging techniques.

2. Results and Discussion

Visualization of fiducial markers in 2D X-ray imaging requires high electron density within the nanogel to possess efficient X-ray attenuation/radio-opacity, which can be achieved by doping the injectable gel with colloid AuNPs. We recently exploited the use of PEG-coated AuNPs but due to the high hydrophilicity of the PEG-coated AuNPs only 10 mg AuNPs mL^{-1} could be included in the liquid marker, which was insufficient for 2D X-ray visibility. Higher AuNP-concentrations resulted in a significant burst release due to the higher preference of the hydrophilic PEG-coated AuNPs for the surrounding aqueous phase.[17]

2.1. Engineering AuNPs for Enhanced Nanogel Compatibility

In order to increase the concentration of AuNPs and enhance the compatibility of the AuNPs with the hydrophobic SAIB-based gelation matrix, two different strategies were investigated: i) Masking the AuNPs by chemisorption of a dithiolane SAIB derivate ($(SH)_2$-SAIB) (**5**) (see Section 2.1.1, and Supporting Information) and ii) using commercially available thiol-functionalized PNIPAM with a molecular weight of 3.500 Da (SH-$PNIPAM_{3.500}$). Both strategies resulted in hydrophobic AuNPs, which was anticipated to reduce the previously observed AuNP burst release from the nanogels. Hence, we hypothesized that realization of one or both of these strategies should enable formulation of nanogels with higher concentrations of AuNPs resulting in higher X-ray contrast levels.

2.1.1. Synthesis of SAIB-Based Capping Agent for AuNP Functionalization

The dithiolane-functionalized SAIB derivate **5** was prepared as outlined in Scheme S1 (Supporting Information) starting from sucrose (**1**). Mono silyl protection of the 6′-OH position of the fructofuranose unit was achieved using *tert*-butyl(chloro)diphenylsilane (TBDPS-Cl) and 4-dimethylaminopyridine (DMAP) yielding 6′-O-TBDPS-sucrose (**2**).[26] The remaining hydroxyl groups were isobutyrylated using isobutyric anhydride and DMAP resulting hepta-isobutyryl-6′-O-TBDPS-sucrose (**3**). Initial attempts of deprotection of the TBDPS group using

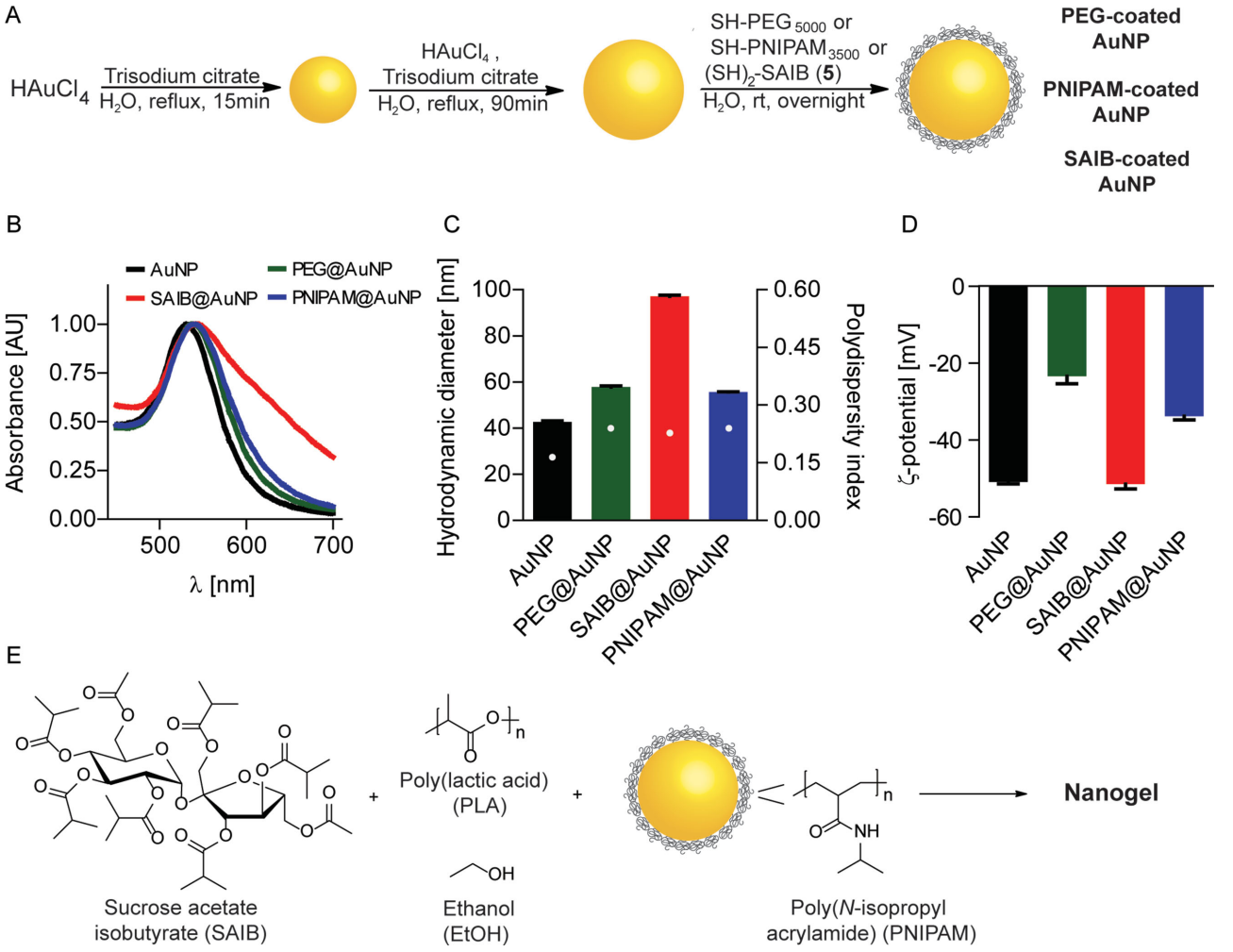

Figure 1. A) Synthesis protocol for obtaining PEG-, PNIPAM, and SAIB-coated AuNPs based on a three steep seeding protocol using chloroauric acid as Au^{3+} source and trisodium citrate as reductant and stabilizer; B) UV–vis characterization of PEG-, PNIPAM-, and SAIB-coated AuNPs in aqueous solution; C) DLS characterization of PEG-, PNIPAM-, and SAIB-coated AuNPs in aqueous solution; and D) ζ-potential characterization of PEG-, PNIPAM-, and SAIB-coated AuNPs in aqueous solution. E) Nanogel composition and preparation procedure.

tetra-n-butylammonium fluoride (TBAF) indicated a high degree of isobutyryl migration; fortunately, this could be suppressed by addition of acetic acid leading to hepta-isobutyryl-sucrose (**4**). Finally, the dithiolane moiety was introduced by *N*-(3-dimethylaminopropyl)-*N′*-ethylcarbodiimide (EDC) activation of lipoic acid in the presence of DMAP yielding the dithiolane-functionalized SAIB derivate **5** (a detailed description of synthesis and compound characterization is available as Supporting Information).

2.1.2. AuNP Synthesis, Functionalization, and Characterization

Citrate-stabilized AuNPs were synthesized using a seeding procedure as previously described resulting in uniform electrostatic-stabilized AuNPs with a diameter of approximately 40 nm.[17] Subsequently, chemisorption of SH-PEG_{5000}, SH-$PNIPAM_{3500}$ or $(SH)_2$-SAIB (**5**) to the citrate-stabilized AuNPs was conducted in aqueous solution in order to increase the colloid compatibility with SAIB-based gels (**Figure 1**A). Increasing the compatibility of the AuNPs with the SAIB-matrix includes increasing the hydrophobicity of the particles. However, a delicate balance exists where the hydrophobicity of the particles is increased without compromising their stability in aqueous solution during synthesis. As evident from the UV–vis (Figure 1B) and dynamic light scattering (DLS) (Figure 1C) analysis, AuNP coating with PEG and PNIPAM was successful. Only a slight increase in the surface plasmon resonance was observed, which is expected due to the microenvironmental changes on the surface of the particles. Additionally, DLS confirmed the presence of the two polymers at the colloid interface since an increase of 15.1 and 12.9 nm was observed for the PEG-coated and PNIPAM-coated AuNPs, respectively. However, chemisorption of $(SH)_2$-SAIB (**5**) to the surface of the electrostatic-stabilized AuNPs caused considerably aggregation due to the poor aqueous solubility of the formed particles, even under the very diluted conditions used. The aggregates formed from SAIB-coated AuNPs were isolated but redispersion in organic solvents such as absolute ethanol was not possible; thus, this class of particles was not investigated further. Synthesis and

subsequently coating of AuNPs with $(SH)_2$-SAIB (**5**) in pure organic solvent using the Burst–Shiffin method may be feasible, but this was not attempted due to the small size of particles formed by this method (<10 nm) and the fact that non-biocompatible solvents such as toluene and toxic phase-transfer agents have to be used, which could limit their use in biological settings.[27]

Additionally, handling of PNIPAM-coated AuNPs was found to be superior compared to PEG-coated AuNPs as these could be lyophilized and stored for prolonged time as an air stabile nanopowder, which readily dispersed into MQ-H_2O and a wide range of protic- and aprotic organic solvents including anhydrous ethanol without causing any changes to particle morphology (Figure S1, Supporting Information). This enabled easy up-concentration, storage, and nanogel formulation compared to the previous described method where AuNPs were transferred into anhydrous EtOH by centrifugation prior to use.

2.2. Contrast Evaluation for 2D X-Ray Visualization of Nanogel in Humans

In order to evaluate the required concentration of AuNPs within the nanogel for visibility on 2D X-rays images in humans, a simulation of 2D digitally reconstructed radiographs (DRRs) was performed based on clinical 3D CT-data for a patient diagnosed with lung cancer. A lung tumor model was chosen as this region is considered as a worst-case scenario due to the high concentration of bone structure in the thoracic region. A simulated nanogel (500 µL) was digitally placed inside the lung tumor of the patient and the specified HU contrast level was varied from 500 to 2000 HU with increments steps of 500 HU on the 3D CT-data. 2D DRRs were created for all angles entering perpendicular around the patient in steps of 5° using a ray-tracing algorithm[28,29] resulting in 72 simulated projections for each contrast level (**Figure 2**). The center position of the DRRs was chosen to be in the center of the simulated nanogel placed centrally within the lung tumor of the patient. On the resulting DRRs, the visibility for each contrast level was evaluated by a contrast-to-noise ratio (CNR) approach, where a region of interest (ROI) for one projection and contrast level was contoured to define the nanogel and then transferred to all other projections. The mean intensity (M_m) and standard deviation (σ_m) of ROIs were calculated and compared to the mean

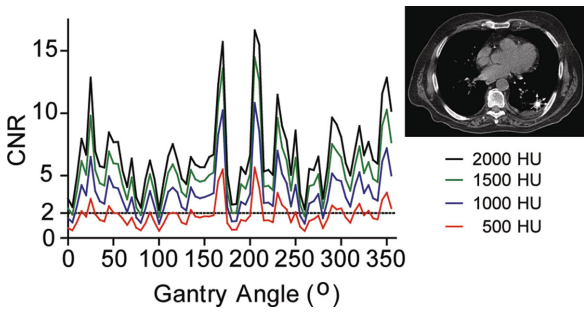

Figure 2. Contrast to noise (CNR) level versus angle of entrance for a simulated nanogel (500 µL) with various contrast levels (500–2000 HU) placed digitally inside a lung tumor.

(M_b) and standard deviation (σ_b) from a ROI on a DRR with no simulated nanogel present according to a CNR evaluation (Equation (1)).

$$\mathrm{CNR} = \frac{|M_m - M_b|}{\sqrt{\sigma_m^2 - \sigma_b^2}} \quad (1)$$

The CNR level can be considered a quantitative measurement of the visibility of the object measured compared to the background contrast from the surroundings. Generally, high CNR translate to increased visibility of the marker. We considered the simulated nanogel visible in the 2D DRR if CNR > 2. This value corresponds to a significance level of 0.05 obtained from a two-tailed *t*-test with a large number of degrees-of-freedom.[30] As evident from Figure 2, some angles requires a higher X-ray contrast level of the nanogel in order to obtain a CNR > 2 as these penetrates bone structure prior to reaching the nanogel. Other angles are more easily accessible and thereby result in lower background contrast, thus making the nanogel more visible on the 2D DRRs. Based on the lung cancer patient projection simulation on the DRRs, it was evident that the contrast level required for CNR > 2 in 95% of all perpendicular angles was approximately 1000 HU (spherical nanogel with a total volume of 500 µL) corresponding to a nanogel with approximately 30 mg AuNPs mL^{-1}. A comparison of the 2D X-ray contrast level from PNIPAM-coated AuNPs (10, 30, 60, and 90 mg mL^{-1}) and clinically used solid fiducial markers is provided in Figure S2, Supporting Information.

2.3. In Vitro Evaluation of Nanogel Performance

In vitro release kinetics of encapsulated PEG-coated and PNIPAM-coated AuNPs in SAIB nanogels doped with polylactic acid (PLA) with the composition SAIB/EtOH/PLA (75:20:5) + 30 mg AuNPs mL^{-1} were examined by placing small droplets (200 µL) of nanogels into MQ-H_2O at physiological temperature. Small aliquots of MQ-H_2O were removed at specific time intervals and replaced with fresh MQ-H_2O to mimic the sink effect in vivo. The amount of released AuNPs was determined by UV–vis spectroscopy using a standard curve of individual synthesized and coated AuNPs with a known concentration (Figure S3, Supporting Information). Injection of nanogel into aqueous solution causes an efflux of EtOH from the nanogel into the aqueous compartment. Efflux of EtOH results in rapid increase in gel viscosity,[24] but may also induce a burst release of encapsulated AuNPs.[24] Indeed, a rapid burst release of PEG-coated AuNPs from nanogels composed of SAIB/EtOH/PLA (75:20:5) + 30 mg PEG-coated AuNPs mL^{-1} was observed. In contrast, the use of PNIPAM-coated AuNPs resulted in highly stable nanogels with no (<1%) AuNP release over time in vitro despite the high AuNP concentration in the gel (Figure S3, Supporting Information). Concentrations as high as 100 mg PNIPAM-coated AuNPs mL^{-1} were evaluated without induced burst release of encapsulated PNIPAM-coated AuNPs (data not shown). The enhanced compatibility of the PNIPAM-coated AuNPs with the SAIB matrix compared to the PEG-coated counterpart can be explained by the enhanced hydrophobicity and potential hydrogen bonding interactions between

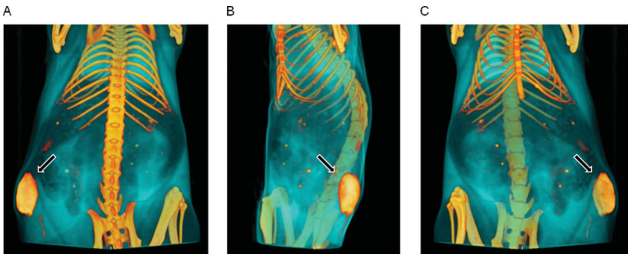

Figure 3. Representative 3D reconstruction from micro-CT images of mouse. Nanogel composed of SAIB/EtOH/PLA (75:20:5) + 30 mg PNIPAM-coated AuNPs mL^{-1} administered subcutaneously to immunocompetent mice at the upper left flank. Nanogel visualized from different angles.

the PNIPAM-coating polymers and the polyester backbone of SAIB. The positive in vitro stability results and known target AuNP concentration for 2D X-ray visibility encouraged us to further evaluate the nanogels composed of SAIB/EtOH/PLA (75:20:5) + 30 mg PNIPAM-coated AuNPs mL^{-1} in vivo using immunocompetent mice.

2.4. In Vivo Evaluation of Nanogel Performance

2.4.1. Evaluation of Nanogel in Immunocompetent Healthy NMRI-Mice

Nanogels (200 µL) composed of SAIB/EtOH/PLA (75:20:5) + 30 mg PNIPAM-coated AuNPs mL^{-1} were injected subcutaneously in immunocompetent NMRI-mice ($n = 5$) at the upper left flank using a 25G needle under general anesthesia. The nanogel was visualized using micro-CT imaging over a period of 8 weeks (images acquired directly after injection and again after 24, 48 h, 1, 2, 4, and 8 weeks) using a dedicated small-animal scanner (**Figure 3**). Based on the recorded micro-CT images, the nanogel X-ray contrast level, degradation rate, and homogeneity were evaluated as a function of time (**Figure 4**). No significant changes in the nanogel volume were observed after the initial EtOH efflux phase, which caused approximately 20% reduction of nanogel volume in good correlation with the known EtOH content of the nanogel prior to injection. The nanogel doped with 30 mg PNIPAM-coated AuNPs mL^{-1} provided a mean X-ray contrast level in the range of 1200 HU, which is sufficient for 2D X-ray visualization as previously described. A reduction of the mean contrast level of the nanogel was observed over time possible due to some AuNP leakage or aggregation of particles within the nanogel. Figure 4B clearly displays the increased maximum contrast level within the nanogel during the first week following intra-gel AuNP aggregation resulting in very high contrast levels (>15.000 HU) (Figure S4, Supporting Information). The homogeneity of the nanogel in terms of PNIPAM-coated AuNP distribution within the gel matrix was analyzed further by investigating each voxel of the micro-CT images as illustrated in Figure 4C. As evident from the cumulative histograms for a representative mouse, the PNIPAM-coated AuNPs were found to gradually aggregate within the nanogel as previously observed for PEG-coated AuNPs within the same gel matrix.[17] In fact, no significant difference was found in the variance of the PEG-coated and PNIPAM-coated AuNPs within the nanogels as analyzed by the Wilcoxon rank-sum test ($p = 0.0734$).[31] The inhomogeneous PNIPAM-coated AuNPs distribution within the nanogel could be visualized in the mice due to the high resolution and small slice thickness ($0.092 \times 0.092 \times 0.092$ mm^3) of the micro-CT scanner. The aggregation phenomenon of the PNIPAM-coated AuNPs within the nanogel has no clinical impact as human clinical scanners operate with significant larger slice thickness (2–3 mm) and lower resolution (1×1 mm^2) causing the AuNP microstructure aggregation to be below the resolution of recorded images.

2.4.2. Evaluation of Nanogel in a Canine Cancer Patient with Spontaneously Developed Solid Tumor

In order to fully validate the concept of liquid injectable fiducial markers for IGRT, the nanogel was evaluated in a canine cancer patient suffering from spontaneously developed malignant solid tumor (mast cell tumor). Solid tumors often show an increased interstitial fluid pressure (IFP) possibly due to vessel abnormalities, fibrosis, and contraction of the interstitial matrix mediated by stromal fibroblasts.[32,33] Increased IFP may serve as an obstacle for intratumoral injection of the developed nanogel as the available intracellular space for marker assembly post-injection is limited and the increased IFP may repel the nanogel into adjacent areas. Additionally, migration of the nanogel over time may compromise the accuracy of fiducial

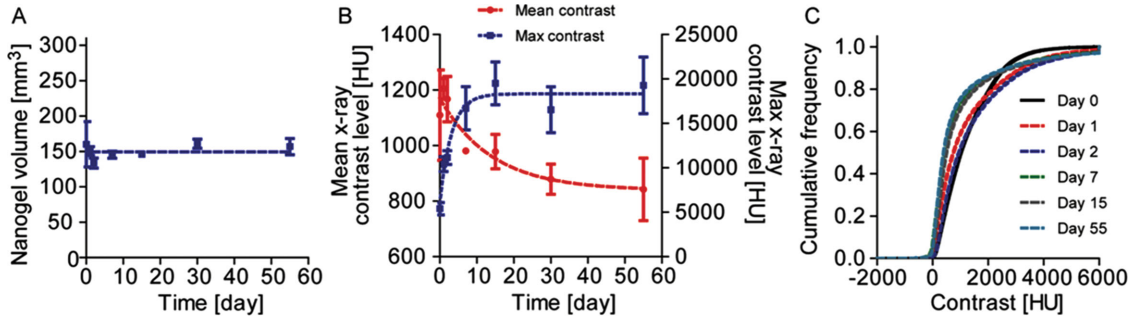

Figure 4. In vivo characteristics of nanogel composed of SAIB/EtOH/PLA (75:20:5) + 30 mg PNIPAM-coated AuNPs mL^{-1} administered subcutaneously to immunocompetent mice at the upper left flank. A) Nanogel degradation over a period of 8 weeks (mean ± SEM, $n = 5$); B) Mean (left axis) and maximum (right axis) X-ray contrast level of nanogel over a period of 8 weeks (mean ± SEM, $n = 5$) and C) Accumulated histogram of nanogel contrast level within each pixel from a representative mouse over a period of 30 d.

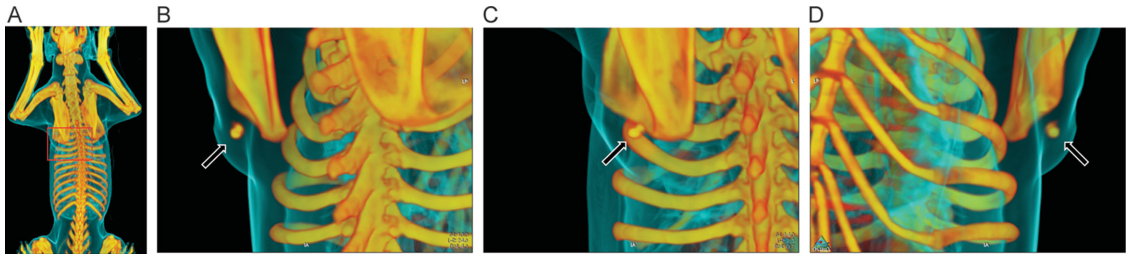

Figure 5. 3D reconstruction based on CT images of canine patient with injected nanogel. Nanogel composed of SAIB/EtOH/PLA (75:20:5) + 30 mg PNIPAM-coated AuNPs mL^{-1} administered intratumorally into a canine suffering from an intermediate-grade subcutaneous mast cell tumor (maximum distance ($x \times y \times z$); $1.82 \times 5.81 \times 5.32$ cm^3, CT volume; 31.64 cm^3) adherent to the underlying soft tissue located over the dorsal aspect of the left shoulder blade. A) Full-body scan of the canine. Area of interest indicated with a red box. B–D) Nanogel visualized from different angles.

marker-based IGRT and potentially result in misguidance of the external radiation beam, which, in turn, leads to poor tumor coverage and increased radiation to healthy adjacent tissue.[16,34] Such obstacles are not encountered for subcutaneous injections of the nanogel as evaluated in immunocompetent NMRI-mice, hence the canine cancer patient with a spontaneously developed solid tumor (mast cell tumor) served as a clinical animal model with high translational value for evaluating the clinical potential of the developed nanogel.

A companion dog (Male, Rhodesian Ridgeback, 10 years, body weight 38 kg) diagnosed with a subcutaneous mast cell tumor (maximum distance ($x \times y \times z$); $1.82 \times 5.81 \times 5.32$ cm^3, CT volume; 31.64 cm^3) adherent to the underlying soft tissue located over the dorsal aspect of the left shoulder blade was given an intratumoral injection of nanogel (300 µL) composed of SAIB/EtOH/PLA (75:20:5) + 30 mg PNIPAM-coated AuNPs mL^{-1} under general anesthesia (**Figure 5**) prior to radiation therapy. Approximately 24 h after the injection of the nanogel, a diagnostic planning CT-scan of the tumor/nanogel region was performed and the therapeutic regimen consisting of four fractions of 6 Gy radiation therapy planned accordingly. Radiation therapy was delivered over 16 d on a clinical linear accelerator equipped with on-board imaging (OBI) capabilities (3D cone beam CT (CBCT) and 2D X-ray imaging).

Prior to each fraction of radiotherapy, CBCT (**Figure 6**) images and 2D X-ray imaging (Figure S5, Supporting Information) were acquired and used for positioning based on nanogel and tumor. Radiation therapy was delivered according to the nanogel position. The size (**Table 1**) and stability of the nanogel in terms of migration and deformation were evaluated based on the recorded CBCT images (Figure 6) by manually contouring the nanogel using 300 HU as a lower threshold. The nanogel size remained constant over the time of treatment with no change in overall volume was observed. The small variations observed in Table 1 are a consequence of motion artifacts from respiratory movement on the recorded CBCT images. Additionally, image analysis revealed that the nanogel retained its 3D shape and was found to be immobilized/associated with the tumor as no migration of the nanogel was observed during the course of radiation therapy despite the canine patient exercising and resting on the tumor inducing mechanical stress on the nanogel. Finally, exposure to four fractions of 6 Gy each was not found to alter the nanogel morphology as evaluated based on the CBCT images. The nanogel was well tolerated and no clinical side effects were observed throughout the study.

3. Conclusion

A novel nanogel composition based on PNIPAM-coated AuNPs formulated in a mixture of SAIB/EtOH/PLA (70:20:5) has been developed. PNIPAM-coated AuNPs were found to be highly compatible with the hydrophobic SAIB-based gel matrix facilitating encapsulation of high concentration of colloidal gold, which enables 2D X-ray visualization of the nanogel. This was confirmed by a simulation of 2D DRRs of a patient suffering from lung cancer. The developed nanogel is the first injectable fiducial marker that can be visualized in 2D X-ray imaging thereby enabling intra- and interfractional IGRT by referencing the nanogel position. The nanogel performance was evaluated

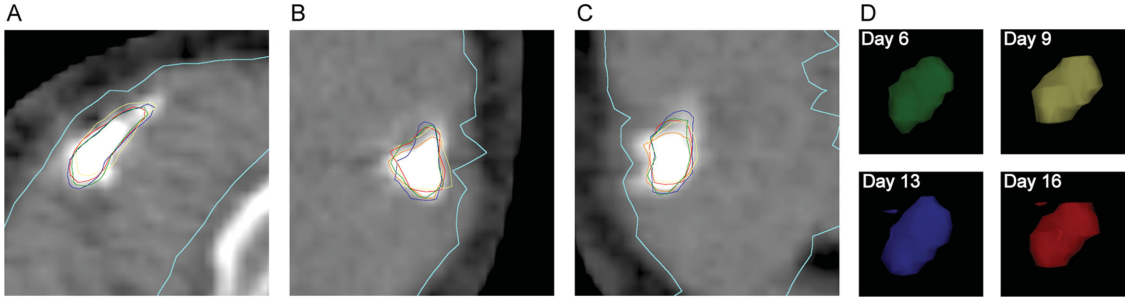

Figure 6. Nanogel composed of SAIB/EtOH/PLA (75:20:5) + 30 mg PNIPAM-coated AuNPs mL^{-1} administered intratumorally into a canine mast cell tumor visualized by CBCT imaging. A) Transversal plane (day 0); B) frontal plane (day 0); C) sagittal plane (day 0). Contours in A–C represent the nanogel on day 6 (green), day 9 (yellow), day 13 (blue), and day 16 (red). The light blue contour represents the gross tumor volume. D) 3D renderings of all the four surfaces represent the nanogel from each day of treatment.

Table 1. Nanogel volume following intratumoral injection in a canine model.

Day #	Nanogel volume [cm^3]
0	0.20
6	0.18
9	0.21
13	0.22
16	0.19

in vivo in immunocompetent mice by subcutaneous injection. Excellent visibility of the nanogel by micro-CT imaging was observed with a mean contrast level of 1200 HU after injection. Over time, the PNIPAM-coated AuNPs were found to form microaggregates within the gel matrix as confirmed by image analysis of the high-resolution micro-CT images. This phenomenon was found to have no clinical impact due to the larger slice thickness of human clinical scanners and lower resolution compared to small animal micro-CT scanners.

The concept of an injectable fiducial marker for use in IGRT was finally validated in a canine cancer patient with a large spontaneous solid tumor. The canine patient provides translational understanding and allowed us to evaluate the clinical potential of the nanogel. The nanogel displayed high image contrast on both conventional CT and CBCT images and could additionally be identified by 2D X-ray imaging, thus providing sufficient radiographic properties for visualization with all the imaging modalities associated with modern linear accelerators. Furthermore, the nanogel retained its size and 3D structure within the tumor microenvironment and no migration of the nanogel was observed within the time period for the radiotherapy treatment procedure. The developed nanogel was utilized to align the canine patient prior to external beam radiation therapy, was found to be unaffected by the deposited radiation dose within the tumor, and no side effects were observed in neither the murine nor the clinically relevant canine model. However, it should be noted that AuNPs are currently not approved for human use and the knowledge about the potential short- and long-term toxicological effects after AuNP exposure is still limited.[36]

The developed nanogel presented in this article is the first liquid fiducial marker, which can be inserted using thin and flexible needles and with a high enough contrast to make it visible in 2D X-ray imaging, which is an important feature for use in IGRT. Furthermore, active pharmaceutical ingredients may be included in the nanogel formulation to improve the therapeutic benefit for the patient, and the AuNPs may enhance the effect of the radiation therapy if the gel is injected directly into tumors.[37,38] In conclusion, the nanogel may provide both human and veterinary radiation oncologists with a new tool for improving planning, alignment, and tumor tracking in radiotherapy and could improve treatment outcome by providing a more precise delivery of the radiation dose to tumors.

4. Experimental Section

Materials: Tetrachloroauric acid trihydrate was purchased from Wako Chemicals GmbH (Neuss, Germany) and MeO-PEG_{5000}-SH was purchased from Rapp Polymere (Tuebingen, Germany). SH-PNIPAM (M_w = 3500Da, PDI = 1.24) was purchased from Polymer Source Inc. (Dorval, Canada). All other chemicals including SAIB, PLA (M_w = 10–18 kDa), trisodium citrate dihydrate, Au-standard for inductively coupled plasma atomic emission spectroscopy (ICP-AES) (1000 mg L^{-1}), hydrochloride acid and nitric acid were purchased from Sigma–Aldrich (Schnelldorf, Germany). All chemicals were used as received from the manufacturer.

*Synthesis of $(SH)_2$-SAIB (**5**)*: $(SH)_2$-SAIB (**5**) was synthesized over four steps starting from sucrose (**1**) in an overall yield of 27%. Full synthetic procedure including chemical characterization (^1H NMR, ^{13}C NMR, HRMS, and FTIR) is available in the Supporting Information.

AuNP Synthesis and Characterization: AuNPs were synthesized as previously described using a two-step seeding procedure resulting in citrate-stabilized AuNPs with an average diameter of 40 nm.[17] The citrate-stabilized AuNPs were subsequently coated with either SH-PEG_{5000}, SH-$PNIPAM_{3500}$, or $(SH)_2$-SAIB (**5**) using eight molecules per nm^2 surface area. Chemisorption of coating materials was in all cases conducted overnight at RT after which the volume was reduced to approximately 15 mL by centrifugation (9.500 RPM, 15 min). The PEG-coated AuNPs, PNIPAM-coated AuNPs, and SAIB-coated AuNPs colloid solutions were washed with MQ-H_2O (3 × 15 mL) and the finally up-concentrated to approximately 75 mg Au mL^{-1} as determined by ICP-MS using an ICP-MS Au standard (1000 mg L^{-1}) as reference. Colloid solutions (citrate-stabilized AuNPs, PEG-, PNIPAM-, and SAIB-coated AuNPs) were furthermore characterized by UV–vis spectrometry, DLS, and ζ-potential measured. PNIPAM-coated AuNPs were finally characterized by TEM (Figure S2, Supporting Information).

Nanogel Formulation: SAIB (1.75 g, 90 w/w% in EtOH) and PLA (105 mg) were mixed and homogenized by a ball homogenizer (frequency 30 s^{-1}, 30 min) to give a clear homogenous solution. Lyophilized PNIPAM-coated AuNPs (63 mg) was weighed off and redispersed into anhydrous EtOH (310 µL) by extensive vortexing and added to the SAIB/PLA mixture to give a final nanogel forming matrix composed of SAIB/EtOH/PLA (75:20:5) with 3.0 w/w% (30 mg mL^{-1}) PNIPAM-coated AuNPs. Formed nanogels were stored at RT and used within 4 h from preparation with vortexing prior to use. Nanogels with PEG-coated AuNPs were prepared as described elsewhere.[17]

*In Vitro Release of PNIPAM- and PEG-*Coated *AuNPs from Nanogel*: Nanogels composed of SAIB/EtOH/PLA (75:20:5) with 3.0 w/w% (30.0 mg mL^{-1}) of either PEG- or PNIPAM-coated AuNPs were prepared as described above. Nanogels (200 µL) were added to glass vials containing MQ-H_2O (10.0 mL, 37 °C) and aliquots (1.0 mL) were removed as a function of time and replaced with an equal amount of MQ-H_2O. The release profile from both nanogels was measured by correlating the UV–vis absorbance of the individual AuNPs with a standard curve based on Au-standards of known concentration (5.0–50.0 µg mL^{-1}).

Simulation of CNR in Lung Cancer Patient: 2D DRRs were performed based on clinical 3D CT-data for a patient diagnosed with lung cancer. 2D DRRs were created using the drrCode ray-tracing algorithm available online (https://code.google.com/p/drrsuite/downloads/list). 2D DRRs were created using a source to detector distance of 150 cm and a detector size of 768 × 1024 pixels (identical to a clinical settings). For conversion from HU to attenuation coefficient, a μ_ρ for water was used assuming monochromatic photons of 120 kV. ROI contouring and CNR calculations for the simulated projections were performed in MATLAB (The MathWorks Inc., Natick, MA, USA) using an in-house-developed simulation and analysis tool.

Animal Models (Mice): Immunocompetent 7-week-old female NMRI mice (n = 5) were given a subcutaneous injection (200 µL) of SAIB/EtOH/PLA (75:20:5) + 30 mg mL^{-1} PNIPAM-coated AuNPs using a 25 G needle in the upper left flank of the anesthetized mice. The animals were given free access to food and water and micro-CT scans were recorded over a period of 8 weeks (24, 48 h, 1, 2, 4, and 8 weeks) using a dedicated small-animal MicroCAT II system (Siemens Medical Solutions, Malvern, PA, USA). Micro-CT images were recorded using the following settings; tube voltage of 67 kVp, tube current of 500 µA, 360 rotation steps, an exposure time of 400 ms, and a voxel size of 0.092 × 0.092 × 0.092 mm^3. The animal experiments were approved by the Animal Research Committee of the Danish Ministry of Justice.

Canine: A privately owned companion dog (Male, Rhodesian Ridgeback, 10 years, bodyweight 38 kg) suffering from a spontaneously developed subcutaneous mast cell tumor (maximum distance ($x \times y \times z$); 1.82 × 5.81 × 5.32 cm^3, CT volume; 31.64 cm^3) adherent to the underlying soft tissue located over the dorsal aspect of the left shoulder blade was used as a clinical relevant model. In conjunction with the standard diagnostic procedures, nanogel (300 µL) was manually injected centrally in the tumor using a 23 G needle and 1 mL syringe. Approximately 24 h after the injection of the nanogel, a diagnostic CT scan (Biograph 40, Siemens Medical Solutions, Erlangen, Germany) of the tumor region was performed with the dog under general anesthesia using the following acquisition parameters; 120 kV, 150 mAs, pixel size 0.977 × 0.977 × 1.00 mm^3). As part of the therapeutic procedure radiation therapy was planned according to the tumor histology and imaging characteristic, and a therapeutic regimen consisting of four fractions of 6 Gy radiation treatments was chosen. Radiation therapy was delivered by a linear accelerator (Novalis TX, Varian Medical Systems, Palo Alto, CA, USA) with on-board imaging capabilities (Cone Beam CT and 2D X-ray imaging) and orthogonal ExacTrac radiography (Brainlab AG, Feldkirchen, Germany). No side effects were observed throughout the study. The canine cancer patient study was approved by the Ethics and Administrative Committee at the Department of Veterinary Clinical and Animal Sciences, Faculty of Health and Medical Sciences, University of Copenhagen, Denmark.

Analysis of Nanogel Homogeneity: The nanogels were delineated by hand using ITK-SNAP.[35] All data analyses were done in MATLAB (The MathWorks Inc., Natick, MA, USA) using in-house- developed software. Based on the voxel values in the gels mean and max values, as well as cumulative histograms were calculated. The cumulative histograms were used for homogeneity evaluation, as changes in the AuNP distribution are reflected in the voxels values and thus the histograms.

Supporting Information

Supporting Information is available from the Wiley Online Library or from the author.

Acknowledgements

This work has been funded by the Technical University of Denmark (DTU), the Niels Bohr Institute, the Danish Council for Strategic Research (Nanoguide, application no. 0603-00442B), and the Novo Foundation.

Received: October 17, 2014
Revised: December 3, 2014
Published online: January 21, 2015

[1] R. Baskar, K. A. Lee, R. Yeo, K. Yeoh, *Int. J. Med. Sci.* **2012**, *9*, 193.
[2] L. A. Dawson, M. B. Sharpe, *Lancet Oncol.* **2006**, *7*, 848.
[3] J. Bussink, J. H. A. M. Kaanders, W. T. A. van der Graaf, W. J. G. Oyen, *Nat. Rev. Clin. Oncol.* **2011**, *8*, 233.
[4] D. Verellen, R. M. De, N. Linthout, K. Tournel, G. Soete, G. Storme, *Nat. Rev. Cancer* **2007**, *7*, 949.
[5] K. M. Langen, D. T. Jones, *Int. J. Radiat. Oncol. Biol. Phys.* **2001**, *50*, 265.
[6] H. Shirato, Y. Seppenwoolde, K. Kitamura, R. Onimura, S. Shimizu, *Semin. Radiat. Oncol.* **2004**, *14*, 10.
[7] P. Giraud, E. Yorke, S. Jiang, L. Simon, K. Rosenzweig, G. Mageras, *Cancer Radiother.* **2006**, *10*, 269.
[8] M. Falk, P. M. af Rosenschold, P. Keall, H. Cattell, B. C. Cho, P. Poulsen, S. Povzner, A. Sawant, J. Zimmerman, S. Korreman, *Radiother. Oncol.* **2010**, *94*, 218.
[9] D. P. Harley, W. S. Krimsky, S. Sarkar, D. Highfield, C. Aygun, B. Gurses, *Ann. Thorac. Surg.* **2010**, *89*, 368.
[10] M. Imura, K. Yamazaki, H. Shirato, R. Onimaru, M. Fujino, S. Shimizu, T. Harada, S. Ogura, H. Dosaka-Akita, K. Miyasaka, M. Nishimura, *Int. J. Radiat. Oncol. Biol. Phys.* **2005**, *63*, 1442.
[11] D. J. Moseley, E. A. White, K. L. Wiltshire, T. Rosewall, M. B. Sharpe, J. H. Siewerdsen, J. Bissonnette, M. Gospodarowicz, P. Warde, C. N. Catton, D. A. Jaffray, *Int. J. Radiat. Oncol. Biol. Phys.* **2007**, *67*, 942.
[12] I. Gauthier, J. Carrier, D. Beliveau-Nadeau, B. Fortin, D. Taussky, *Int. J. Radiat. Oncol. Biol. Phys.* **2009**, *74*, 1128.
[13] R. Khosa, S. Nangia, K. S. Chufal, D. Ghosh, R. Kaul, L. Sharma, *J. Cancer Res. Ther.* **2010**, *6*, 172.
[14] S. Yousefi, B. T. Collins, C. A. Reichner, E. D. Anderson, C. Jamis-Dow, G. Gagnon, S. Malik, B. Marshall, T. Chang, F. Banovac, *Clin. Lung Cancer* **2007**, *8*, 252.
[15] N. Kothary, J. J. Heit, J. D. Louie, W. T. Kuo, B. W. J. Loo, A. Koong, D. T. Chang, D. Hovsepian, D. Y. Sze, L. V. Hofmann, *J. Vasc. Interv. Radiol.* **2009**, *20*, 235.
[16] N. Bhagat, N. Fidelman, J. C. Durack, J. Collins, R. L. Gordon, J. M. LaBerge, R. K. J. Kerlan, *Cardiovasc. Interv. Radiol.* **2010**, *33*, 1186.
[17] R. I. Jølck, T. Binderup, A. E. Hansen, J. B. Scherman, P. M. af Rosenschold, A. Kjær, T. L. Andresen, *Adv. Healthcare Mater.* **2014**, *3*, 1680.
[18] H. Shirato, K. Suzuki, G. C. Sharp, K. Fujita, R. Onimaru, M. Fujino, N. Kato, Y. Osaka, R. Kinoshita, H. Taguchi, S. Onodera, K. Miyasaka, *Int. J. Radiat. Oncol. Biol. Phys.* **2006**, *64*, 1229.
[19] T. Juhler-Nottrup, S. S. Korreman, A. N. Pedersen, G. F. Persson, L. R. Aarup, H. Nystrom, M. Olsen, N. Tarnavski, L. Specht, *Acta Oncol.* **2008**, *47*, 1406.
[20] S. S. Korreman, T. Juhler-Nottrup, G. F. Persson, P. A. Navrsted, M. Enmark, H. Nystrom, L. Specht, *Acta Oncol.* **2008**, *47*, 1390.
[21] M. L. Taylor, T. Kron, R. D. Franich, *Acta Oncol.* **2011**, *50*, 483.
[22] C. Rubio, O. Hernando, R. Morera, T. Leroy, S. E. Lartigau, *Rep. Pract. Oncol. Radiother.* **2013**, *18*, 387.
[23] Y. Lu, H. He, Y. Cui, X. Tang, *Yao Xue Xue Bao.* **2007**, *42*, 445.
[24] Y. Lu, Y. Yu, X. Tang, *J. Pharm. Sci.* **2007**, *96*, 3252.
[25] X. Lin, S. Yang, J. Gou, M. Zhao, Y. Zhang, N. Qi, H. He, C. Cai, X. Tang, P. Guo, *J. Mater. Sci.: Mater. Med.* **2012**, *23*, 443.
[26] M. M. Andrade, M. T. Barros, *Tetrahedron* **2004**, *60*, 9235.
[27] M. Brust, M. Walker, D. Bethell, D. J. Schiffrin, R. Whyman, *Chem. Commun.* **1994**, *7*, 801.
[28] F. Jacobs, E. Sundermann, B. De Sutter, M. Christiaens, I. Lemahieu, *J .Comput. Inf. Technol.* **1998**, *6*, 89.
[29] R. L. Siddon, *Phys. Med. Biol.* **1985**, *30*, 817.
[30] Y. Chen, J. J. O'Connell, C. J. Ko, R. R. Mayer, A. Belard, J. E. McDonough, *Phys. Med. Biol.* **2012**, *57*, 155.
[31] F. Wilcoxon, *J. Econ. Entomol.* **1946**, *39*, 269.
[32] C. Heldin, K. Rubin, K. Pietras, A. Oestman, *Nat. Rev. Cancer* **2004**, *4*, 806.
[33] P. Vaupel, *Semin. Radiat. Oncol.* **2004**, *14*, 198.
[34] J. C. Hong, N. C. W. Eclov, Y. Yu, A. K. Rao, S. Dieterich, Q. Le, M. Diehn, D. Y. Sze, B. W. Loo Jr., N. Kothary, P. G. Maxim, *J. Appl. Clin. Med. Phys.* **2013**, *14*, 4046.
[35] P. A. Yushkevich, J. Piven, H. C. Hazlett, R. G. Smith, S. Ho, J. C. Gee, G. Gerig, *Neuroimage* **2006**, *31*, 1116.
[36] A. Gerber, M. Bundschuh, D. Klingelhofer, D. A. Groneberg, *J. Occup. Med. Toxicol.* **2013**, *8*, 32.
[37] X. Zhang, D. Wu, X. Shen, J. Chen, Y. Sun, P. Liu, X. Liang, *Biomaterials* **2012**, *33*, 6408.
[38] X. Zhang, J. Chen, Z. Luo, D. Wu, X. Shen, S. Song, Y. Sun, P. Liu, J. Zhao, S. Huo, S. Fan, F. Fan, X. Liang, J. Xie, *Adv. Healthcare Mater.* **2014**, *3*, 133.